

A Stochastic Projection Method for Fluid Flow

I. Basic Formulation

Olivier P. Le Maître,* Omar M. Knio,^{†1} Habib N. Najm,[‡] and Roger G. Ghanem[§]

*Centre d'Etudes de Mécanique d'Ile de France, Université d'Evry Val d'Essone, 40, rue du Pelvoux, 91020 Evry Cedex, France; [†]Department of Mechanical Engineering, The Johns Hopkins University, Baltimore, Maryland 21218-2686; [‡]Combustion Research Facility, Sandia National Laboratories, Livermore, California 94550; and [§]Department of Civil Engineering, The Johns Hopkins University, Baltimore, Maryland 21218-2686
E-mail: olm@iup.univ-evry.fr; knio@jhu.edu; hnnajm@ca.sandia.gov; ghanem@jhu.edu

Received November 7, 2000; revised July 10, 2001

We describe the construction and implementation of a stochastic Navier–Stokes solver. The solver combines a spectral stochastic uncertainty representation scheme with a finite difference projection method for flow simulation. The uncertainty quantification scheme is adapted from the spectral stochastic finite element method (SSFEM), which is based on regarding uncertainty as generating a new dimension and the solution as being dependent on this dimension. In the SSFEM formalism, the stochastic dependence is represented in terms of the polynomial chaos system, and the coefficients in the corresponding spectral representation are obtained using a Galerkin approach. It is shown that incorporation of the spectral uncertainty representation scheme into the projection method results in a coupled system of advection–diffusion equations for the various uncertainty fields, and in a *decoupled* system of pressure projection steps. This leads to a very efficient stochastic solver, whose advantages are illustrated using steady and transient simulations of transport and mixing in a microchannel. © 2001 Academic Press

Key Words: stochastic; Navier–Stokes; polynomial chaos; uncertainty.

1. INTRODUCTION

Simulation of complex physical systems is in many instances made more difficult by various uncertainties, which may include inexact knowledge of system forcing, initial and boundary conditions, and parametric uncertainties in the physical model and in physical properties of the medium. The latter may exhibit a random component with significant spatial

¹ Corresponding author.

or temporal fluctuations, or may be inaccurately known. An example concerns chemical or biological microfluid systems, whose modeling involves complex kinetic mechanisms which may include dozens of species—each characterized by thermodynamic and transport properties—and hundreds of elementary reactions specified in terms of rate parameters. Thus, simulation and design of these microdevices, which is the primary motivation behind the present effort, involve complex physical models having a large number of parameters that may be known in an approximate fashion only. Consequently, in order to become effective tools, it is essential for simulation-based design approaches to include a rational assessment of uncertainty.

Uncertainty quantification is typically based on Monte Carlo (MC) techniques [1, 2] that essentially amount to performing deterministic simulations for randomly selected conditions, and then conducting a statistical analysis on the resulting set of realizations in order to extract the relevant statistical properties of the process. The Monte Carlo approach is known to be robust and to be able to deal with very complex situations. However, because of CPU costs and storage limitations, this approach is often restricted to problems involving a small number of uncertain parameters and/or degrees of freedom.

In this work an alternative approach is adopted which is adapted from the spectral stochastic finite element method (SSFEM) [3]. The essential concept in SSFEM is to regard uncertainty as generating a new dimension and the solution as being dependent on this dimension. A convergent expansion along the new dimension is then sought in terms of the polynomial chaos system [4, 5], and the coefficients in this representation are determined through a Galerkin approach. SSFEM offers several advantages over MC approaches; in particular, it generally results in efficient uncertainty propagation schemes and yields quantitative estimates of the sensitivity of the solution with respect to uncertainties in model data. In addition, this quantitative information is expressed in a format that permits it to be readily used to probe the dependence of specific observables on particular components of the input data, to design experiments in order to better calibrate and test the validity of postulated models, or to assess “off-design” performance. SSFEM has been used in various applications, including structural mechanics problems (e.g., [3, 6]) and flow in random porous media (e.g., [7, 8]). A modified SSFEM approach has been recently applied to complex kinetic mechanisms [9], but this method has not yet been used in more general fluid problems.

Note, however, that the polynomial chaos expansions on which SSFEM is based have been used in various contexts, for instance in the development of variance reduction or convergence acceleration techniques [10–12], and also in the analysis of turbulent velocity fields [13–15]. In particular, the analysis of Chorin [15] indicates that in complex problems involving shock formation or an energy cascade, polynomial chaos expansions may lose their advantages or cease to be useful. Such difficulties do not arise in the present work, which aims at adapting the stochastic representation formalism to microfluid applications at a low Reynolds number.

As summarized in Section 2, we restrict our attention in this paper to the case of advection and mixing in two-dimensional, incompressible flow. Specifically, we focus on a class of simplified problems in which the uncertainty in the solution process arises as a result of either random viscosity or the dependence of the viscosity on a random temperature. We first start with a simplified setting in which the temperature is treated as a Gaussian random variable that is spatially uniform. Thus, the fluid viscosity is also uniform, but both linear and nonlinear viscosity laws are considered in the analysis. A more complicated setting is then

considered, which consists of a double-inlet channel where the inlet temperature of one of the streams has a random Gaussian component. In this case, the uncertain boundary condition leads to stochastic velocity and temperature fields that are coupled by the temperature dependence of viscosity.

In Section 3, a spectral uncertainty representation scheme is introduced based on the decomposition of the solution process in terms of the polynomial chaos system. This representation is then introduced into the original system of equations, and a Galerkin procedure is used to determine the coefficients in the spectral expansion. It is shown that this approach results in a coupled system of advection–diffusion equations for the stochastic velocity (and temperature) fields, with a decoupled set of stochastic divergence constraints. This feature is then exploited in Section 4 by constructing an efficient stochastic projection method (SPM) which provides a stochastic characterization of the solution process at a cost that is essentially proportional to the number of terms in the spectral expansion. The advantages of the stochastic projection method (SPM) are illustrated in Section 5 in light of computational experiments conducted for the model problems introduced in Section 3. Major conclusions are given in Section 6.

2. GOVERNING EQUATIONS

We consider the two-dimensional flow, in (x, y) plane, of an incompressible, uniform-density Newtonian fluid inside a narrow channel of height H and width B . As shown in Fig. 1, the boundaries of the computational domain Ω consist of inflow (Γ_i) and outflow (Γ_o) boundaries, respectively located at $y = 0$ and $y = H$, and solid boundaries (Γ_{ns}) located at $x = 0$ and $x = B$.

The evolution of the flow within the channel is governed by the Navier–Stokes equations

$$\begin{aligned} \frac{\partial \mathbf{u}}{\partial t} + (\mathbf{u} \cdot \nabla) \mathbf{u} &= -\nabla p + \nabla \cdot \bar{\boldsymbol{\sigma}} & \text{(a)} \\ \nabla \cdot \mathbf{u} &= 0 & \text{(b),} \end{aligned} \tag{1}$$

where \mathbf{u} is the velocity field, \tilde{p} is the pressure, ρ is the density, $p \equiv \tilde{p}/\rho$, $\boldsymbol{\tau}$ is the viscous stress, and $\bar{\boldsymbol{\sigma}} \equiv \boldsymbol{\tau}/\rho$. When the dynamic viscosity is uniform, the viscous force can be

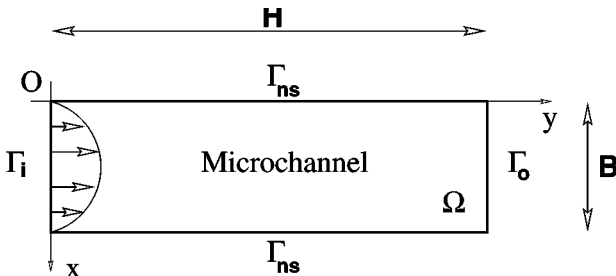


FIG. 1. Schematic representation of the computational domain. The inflow and outflow boundaries, respectively Γ_i and Γ_o , are located at $y = 0$ and $y = H$. Γ_{ns} refers to the channel walls, which are located at $x = 0$ and $x = B$. The computational domain consists of the region $\Omega \equiv [0, B] \times [0, H]$.

expressed as

$$\nabla \cdot \bar{\sigma} \equiv \nabla \cdot [v\bar{S}] = v\nabla^2 \mathbf{u}, \quad (2)$$

where v is the kinematic viscosity and \bar{S} is the symmetric part of the velocity gradient tensor. The governing equations are supplemented with velocity boundary conditions, which consist of imposed velocity at the inflow, outflow conditions on Γ_o , and no-slip conditions on the solid walls.

In addition to the Navier–Stokes equations (1), we also consider the temperature distribution within the microchannel. The evolution of the temperature field, T , is governed by the energy equation

$$\frac{\partial T}{\partial t} + \nabla \cdot (\mathbf{u}T) = \nabla \cdot (\lambda \nabla T), \quad (3)$$

where λ is the thermal diffusivity. We use adiabatic conditions at the solid walls, outflow conditions at Γ_o , and Dirichlet conditions at inflow. Note that when the viscosity is independent of temperature, the evolution of the flow field can be determined independently of Eq. (3). On the other hand, when v depends on T , a nontrivial coupling exists between the Navier–Stokes and the energy equations.

3. STOCHASTIC FORMULATION

3.1. Problems and Methodology

As mentioned in the introduction, we focus on the case of uncertain transport properties and boundary conditions, and restrict our attention to stochastic processes generated by Gaussian random variables. Within this restricted scope, three different problems of increasing complexity are considered:

1. In the first problem (P1), we consider the case of an uncertain viscosity, which is treated as a Gaussian random variable. The viscosity is assumed to be spatially uniform, and solution of the energy equation is not required.
2. In the second problem (P2), we also consider uncertainty in viscosity, which is taken to be generated by a Gaussian stochastic temperature. The temperature is assumed to be uncertain, but spatially uniform, and the uncertainty in viscosity is reflected through a nonlinear viscosity law.
3. In the third problem (P3), we consider a coupled problem which involves a temperature-dependent viscosity and an evolving temperature field. In this case, the uncertainty is generated by a random boundary condition on the inlet temperature.

As mentioned in the introduction, we develop a spectral representation of the stochastic processes, following the approach outlined in [3]. The methodology is based on a two-step procedure; first, the uncertain data is expressed in terms of a “normalized” Gaussian random variable ξ . The dependence of the solution process on ξ is then expanded in terms of the polynomial chaos system. In the present case, a single random variable is considered so the polynomial chaos basis functions are orthogonal Hermite polynomials in the random variable ξ . This spectral expansion is introduced into the governing equations and the coefficients are determined using a weighted residual procedure.

3.2. Statement of P1

As mentioned earlier, for this problem the uncertain viscosity coefficient is spatially uniform and is modeled as a Gaussian random variable. The governing equations consist of the momentum and continuity equations

$$\frac{\partial \mathbf{u}}{\partial t} + (\mathbf{u} \cdot \nabla) \mathbf{u} = -\nabla p + \nu \nabla^2 \mathbf{u} \tag{4}$$

$$\nabla \cdot \mathbf{u} = 0, \tag{5}$$

with deterministic boundary conditions on the velocity. The viscosity is expressed as

$$\nu = \nu_0 + \xi_1 \nu_1, \tag{6}$$

where ν_0 is the mean viscosity, ξ_1 is a “normalized” Gaussian variable (having with zero mean and unit variance), while ν_1 is a deterministic coefficient which corresponds to the standard deviation of the viscosity.

Remark. The index on ξ is introduced in order to emphasize the fact that the present approach can be extended to the situation where ν is a random process with spatial variation. In this case, we rely on the Karhunen–Loève expansion to decompose ν as [16],

$$\nu(\mathbf{x}) = \nu_0(\mathbf{x}) + \sum_{i=1}^L \lambda_i \nu_i(\mathbf{x}) \xi_i,$$

where the λ_i 's are deterministic coefficients, the ξ_i 's are orthogonal (uncorrelated) Gaussian random variables, the functions $\nu_i(\mathbf{x})$ are the eigenvalues of the viscosity autocorrelation function, and L is the order of the expansion. While we do not address this situation in the present work, we still retain the notation of the more general case. Also note that with the use of Gaussian noise in the viscosity, negative values are, in principle, possible. Below, this situation avoided by ensuring that the standard deviation in viscosity is substantially smaller than the mean. In more general situations, a non-Gaussian distribution may be needed to ensure that negative viscosities have negligible likelihood.

The dependence of the solution on the stochastic viscosity is expressed by expanding the velocity and pressure fields as

$$\mathbf{u}(\mathbf{x}) = \sum_{i=0}^P \mathbf{u}_i(\mathbf{x}) \Psi_i(\xi_1) \tag{7}$$

$$p(\mathbf{x}) = \sum_{i=0}^P p_i(\mathbf{x}) \Psi_i(\xi_1), \tag{8}$$

where the Ψ_i denote the polynomials chaoses in the random variable ξ_1 , \mathbf{u}_i and p_i are (yet undetermined) deterministic coefficients, and P is the order of the polynomial chaos expansion. Expressions for Ψ_i (in the case of a single Gaussian random variable) are provided in the Appendix. The effect of the expansion order, P , is analyzed in Section 5.2.

Next, we introduce the polynomial chaos expansions (7 and 8) into the governing equations (4 and 5), which results in

$$\sum_{i=0}^P \Psi_i \frac{\partial \mathbf{u}_i}{\partial t} + \sum_{i=0}^P \sum_{j=0}^P (\mathbf{u}_i \cdot \nabla) \mathbf{u}_j \Psi_i \Psi_j = - \sum_{i=0}^P \Psi_i \nabla p_i + (v_0 + v_1 \xi_1) \nabla^2 \sum_{i=0}^P \Psi_i \mathbf{u}_i \quad (9)$$

$$\sum_{i=0}^P \Psi_i \nabla \cdot \mathbf{u}_i = 0. \quad (10)$$

Multiplying Eq. (9) by Ψ_k and taking the expected value (denoted using the double bracket $\langle \cdot \rangle$) we obtain

$$\begin{aligned} \sum_{i=0}^P \frac{\partial \mathbf{u}_i}{\partial t} \langle \Psi_i \Psi_k \rangle + \sum_{i=0}^P \sum_{j=0}^P (\mathbf{u}_i \cdot \nabla) \mathbf{u}_j \langle \Psi_i \Psi_j \Psi_k \rangle \\ = - \sum_{i=0}^P \nabla p_i \langle \Psi_i \Psi_k \rangle + \sum_{i=0}^P \nabla^2 \mathbf{u}_i \langle (v_0 + v_1 \xi_1) \Psi_i \Psi_k \rangle \quad k = 0, \dots, P. \end{aligned} \quad (11)$$

By virtue of the orthogonality of the polynomial chaos, (11) reduces to

$$\begin{aligned} \frac{\partial \mathbf{u}_k}{\partial t} \langle \Psi_k \Psi_k \rangle + \sum_{i=0}^P \sum_{j=0}^P (\mathbf{u}_i \cdot \nabla) \mathbf{u}_j \langle \Psi_i \Psi_j \Psi_k \rangle \\ = - \nabla p_k \langle \Psi_k \Psi_k \rangle + \sum_{i=0}^P \nabla^2 \mathbf{u}_i \langle (v_0 + v_1 \xi_1) \Psi_i \Psi_k \rangle \quad k = 0, \dots, P. \end{aligned} \quad (12)$$

Dividing by $\langle \Psi_k \Psi_k \rangle$, using the fact that $\Psi_1 = \xi_1$ (see Appendix), and expanding the last term finally leads to the following coupled system of evolution equations for the velocity “modes”:

$$\frac{\partial \mathbf{u}_k}{\partial t} + \sum_{i=0}^P \sum_{j=0}^P (\mathbf{u}_i \cdot \nabla) \mathbf{u}_j \frac{\langle \Psi_i \Psi_j \Psi_k \rangle}{\langle \Psi_k \Psi_k \rangle} = - \nabla p_k + v_0 \nabla^2 \mathbf{u}_k + v_1 \sum_{i=0}^P \nabla^2 \mathbf{u}_i \frac{\langle \Psi_1 \Psi_i \Psi_k \rangle}{\langle \Psi_k \Psi_k \rangle}. \quad (13)$$

We follow a similar treatment for the velocity divergence constraint. Specifically, we multiply Eq. (10) with Ψ_k and then take the expectation to obtain

$$\nabla \cdot \mathbf{u}_k = 0, \quad (14)$$

which in fact corresponds to a weak formulation of the original continuity equation. Boundary conditions and numerical solution schemes will be discussed later.

3.3. Statement of P2

Here, we consider that the viscosity is temperature-dependent and that the temperature T is uncertain and can be modeled as a Gaussian distribution. We let T_0 denote the mean temperature, T_1 the standard deviation, and represent T as

$$T = T_0 + \xi_1 T_1, \quad (15)$$

where ξ_1 is a normalized Gaussian random variable with zero mean. We assume a polynomial representation of the viscosity in the neighborhood of T_0 and restrict our attention to the second-order case

$$\frac{\nu(T)}{\nu_0} = 1 + a_1(T - T_0) + a_2(T - T_0)^2, \quad (16)$$

where a_1 and a_2 are given constants and $\nu_0 \equiv \nu(T_0)$. Substituting Eq. (15) into Eq. (16) we obtain the following stochastic representation for ν :

$$\frac{\nu(T_0 + \xi_1 T_1)}{\nu_0} = 1 + \beta_1 \xi_1 + \beta_2 \xi_1^2, \quad (17)$$

where $\beta_1 \equiv a_1 T_1$ and $\beta_2 \equiv a_2 T_1^2$. It follows that the viscous force in the momentum equation (4) can be written as

$$\nabla \cdot [\nu \bar{\mathcal{S}}] = \nu_0 \nabla \cdot \left[\sum_{i=0}^P (1 + \beta_1 \xi_1 + \beta_2 \xi_1^2) \bar{\mathcal{S}}_i \Psi_i \right], \quad (18)$$

where $\mathbf{u}(\mathbf{x})$ is expanded as in Eq. (7). Multiplying by Ψ_k and taking the expectation we find

$$\langle \nabla \cdot [\nu \bar{\mathcal{S}}] \Psi_k \rangle = \nu_0 \sum_{i=0}^P \nabla^2 \mathbf{u}_i \langle \Psi_i \Psi_k \rangle + \nu_0 \beta_1 \sum_{i=0}^P \nabla^2 \mathbf{u}_i \langle \xi_1 \Psi_i \Psi_k \rangle + \nu_0 \beta_2 \sum_{i=0}^P \nabla^2 \mathbf{u}_i \langle \xi_1^2 \Psi_i \Psi_k \rangle. \quad (19)$$

Using the definitions $\Psi_1 = \xi_1$ and $\Psi_2 = \xi_1^2 - 1$ in Eq. (19) we get

$$\begin{aligned} \langle \nabla \cdot [\nu \bar{\mathcal{S}}] \Psi_k \rangle &= \nu_0 (1 + \beta_2) \nabla^2 \mathbf{u}_k \langle \Psi_k \Psi_k \rangle + \nu_0 \beta_1 \sum_{i=0}^P \nabla^2 \mathbf{u}_i \langle \Psi_1 \Psi_i \Psi_k \rangle \\ &\quad + \nu_0 \beta_2 \sum_{i=0}^P \nabla^2 \mathbf{u}_i \langle \Psi_2 \Psi_i \Psi_k \rangle. \end{aligned} \quad (20)$$

Substituting into the Navier–Stokes equation, we obtain the following coupled system for the velocity and pressure modes:

$$\begin{aligned} \frac{\partial \mathbf{u}_k}{\partial t} + \sum_{i=0}^P \sum_{j=0}^P (\mathbf{u}_i \cdot \nabla) \mathbf{u}_j \frac{\langle \Psi_i \Psi_j \Psi_k \rangle}{\langle \Psi_k \Psi_k \rangle} \\ = -\nabla p_k + \nu_0 (1 + \beta_2) \nabla^2 \mathbf{u}_k + \nu_0 \beta_1 \sum_{i=0}^P \nabla^2 \mathbf{u}_i \frac{\langle \Psi_1 \Psi_i \Psi_k \rangle}{\langle \Psi_k \Psi_k \rangle} \\ + \nu_0 \beta_2 \sum_{i=0}^P \nabla^2 \mathbf{u}_i \frac{\langle \Psi_2 \Psi_i \Psi_k \rangle}{\langle \Psi_k \Psi_k \rangle} \quad k = 0, \dots, P. \end{aligned} \quad (21)$$

As before, the continuity equation results in the divergence constraints $\nabla \cdot \mathbf{u}_k = 0$, $k = 0, \dots, P$.

Note that if $a_2 = 0$, then the viscosity evolves linearly with T , and problem P1 is recovered with the choice $\nu_1 = a_1 T_1$. On the other hand, where $a_2 \neq 0$, it is clear that ν is no longer Gaussian. In the computations, we analyze the effect of non-Gaussian statistics by contrasting linear and nonlinear viscosity laws.

3.4. Statement of P3

In the third problem, the temperature is no longer assumed spatially uniform and its evolution is governed by the energy equation (3). The kinematic viscosity is assumed to vary linearly with temperature, according to

$$\frac{\nu(\mathbf{x})}{\nu_0} = 1 + K'(T(\mathbf{x}) - T_{ref}), \quad (22)$$

where T_{ref} is a reference temperature, $\nu_0 \equiv \nu(T_{ref})$, and K' is a constant. Note that the temperature-dependence of the viscosity provides a nontrivial coupling between the energy and Navier–Stokes equations. The uncertainty in the process is considered to arise as a result of a stochastic temperature profile, T_{in} , at the inlet of the microchannel.

As before, we rely on the polynomial chaos expansion of the stochastic fields

$$T(\mathbf{x}) = \sum_{i=0}^P T_i(\mathbf{x})\Psi_i \quad (23)$$

$$\mathbf{u}(\mathbf{x}) = \sum_{i=0}^P \mathbf{u}_i(\mathbf{x})\Psi_i \quad (24)$$

$$p(\mathbf{x}) = \sum_{i=0}^P p_i(\mathbf{x})\Psi_i \quad (25)$$

$$\nu(\mathbf{x}) = \nu_0(1 - K'T_{ref}) + \nu_0K' \sum_{i=0}^P T_i(\mathbf{x})\Psi_i. \quad (26)$$

Introducing (23) into the energy equation, multiplying by Ψ_k , and evaluating the expectation, we get

$$\frac{\partial T_k}{\partial t} + \sum_{i=0}^P \sum_{j=0}^P \mathbf{u}_i \cdot \nabla T_j \frac{\langle \Psi_i \Psi_j \Psi_k \rangle}{\langle \Psi_k \Psi_k \rangle} = \lambda \nabla^2 T_k \quad k = 0, \dots, P. \quad (27)$$

Analogously, we introduce Eqs. (24)–(26) into Eq. (1) and perform a similar decomposition to obtain

$$\begin{aligned} \frac{\partial \mathbf{u}_k}{\partial t} + \sum_{i=0}^P \sum_{j=0}^P (\mathbf{u}_i \cdot \nabla) \mathbf{u}_j \frac{\langle \Psi_i \Psi_j \Psi_k \rangle}{\langle \Psi_k \Psi_k \rangle} \\ = -\nabla p_k + \nu_0(1 - K'T_{ref})\nabla^2 \mathbf{u}_k \\ + \nu_0K' \sum_{i=0}^P \sum_{j=0}^P \nabla \cdot (T_j \mathcal{S}(\mathbf{u}_i)) \frac{\langle \Psi_i \Psi_j \Psi_k \rangle}{\langle \Psi_k \Psi_k \rangle} \quad k = 0, \dots, P, \end{aligned} \quad (28)$$

with the same velocity divergence constraints as in Eq. (14).

3.5. Treatment of Boundary Conditions

Similar to the treatment of field variables, a “weak formulation” approach is adopted for the boundary conditions. For brevity, we only illustrate this approach for the inflow

condition. As mentioned earlier, the velocity profile is imposed at the channel inlet; we have

$$\mathbf{u}(\mathbf{x} \in \Gamma_i) = \mathbf{u}_{in}, \quad (29)$$

where \mathbf{u}_{in} denotes the deterministic velocity at Γ_i . Expanding the above equation in terms of the polynomial chaos system, we have

$$\mathbf{u}_0(\mathbf{x} \in \Gamma_i) = \mathbf{u}_{in} \quad (30)$$

$$\mathbf{u}_k(\mathbf{x} \in \Gamma_i) = 0 \quad k = 1, \dots, P. \quad (31)$$

Similarly, for the inflow temperature conditions we have

$$T_k(\mathbf{x} \in \Gamma_i) = \langle T_{in} \Psi_k \rangle \quad k = 0, \dots, P. \quad (32)$$

Thus, unlike the inlet velocity profile, the inflow temperature may admit stochastic components whose amplitudes are specified by the right-hand side of Eq. (32). As mentioned in Section 3.4, a random temperature component at inflow results in strong coupling between the momentum and energy equations.

4. SOLUTION METHOD

It can be observed from the previous section that the equation system governing the evolution of the uncertainty modes $\mathbf{u}_k, p_k, k = 0, \dots, P$, has a similar form to the original Navier–Stokes equation. Because of the appearance of coupling terms, however, the system size is by a factor of P larger than the corresponding deterministic system. If not addressed properly, the enlargement of the system size in the stochastic formulation can constitute a major drawback, especially when the implementation of a fast $O(N)$ solver is not possible. Another consideration that has guided the present development is a desire to base the proposed development on existing deterministic solvers and computer codes.

Our approach to the formulation of the stochastic solver is based on the observation that the velocity divergence constraints are *decoupled*, and this suggests the implementation of a projection scheme [17] in which the advection and diffusion terms are integrated in a first fractional step, and the divergence constraints are then enforced in a second fractional step. Because the divergence constraints are decoupled, this approach results in a set of $P + 1$ decoupled pressure projection steps. Since these steps typically account for the bulk of the computational effort in incompressible flow simulations, the solution of the stochastic system can be obtained at essentially a cost of $P + 1$ deterministic solutions. Coupled with the spectral nature of the stochastic representation, this leads to a highly efficient stochastic solver, as illustrated in the examples of the following section. Note that in the case of multiple random variables, the stochastic solution can be determined at a cost essentially of L deterministic solutions, where L is the order of the Karhunen–Loève expansion (Eq. (3.2)). Generally, P and L are generally much smaller than the number of independent MC realizations that are needed for adequate representation of the uncertainty. This feature, together with the decoupled structure of the pressure projection steps, is behind the efficiency of SPM.

The formulation of the stochastic solver adapts elements of previously developed low-Mach-number solvers in [18, 19]. We rely on discretization of all fields variables using a

uniform Cartesian mesh with cell size Δx and Δy in the x - and y -directions, respectively. The velocity modes \mathbf{u}_k are defined on cell edges, while the scalar fields p_k , T_k , and v_k are defined on cell centers. Spatial derivatives are approximated using second-order centered differences.

As mentioned earlier, the governing equations are integrated using a fractional step projection scheme, and the implementation of the scheme is illustrated for the stochastic formulation developed in Section 3.4. In the first fractional step, we integrate the coupled advection–diffusion equations,

$$\begin{aligned} \frac{\partial \mathbf{u}_k}{\partial t} + \sum_{i=0}^P \sum_{j=0}^P (\mathbf{u}_i \cdot \nabla) \mathbf{u}_j \frac{\langle \Psi_i \Psi_j \Psi_k \rangle}{\langle \Psi_k \Psi_k \rangle} \\ = v_0(1 - K' T_{ref}) \nabla^2 \mathbf{u}_k + v_0 K' \sum_{i=0}^P \sum_{j=0}^P \nabla \cdot (T_j \bar{\mathbf{S}}(\mathbf{u}_i)) \frac{\langle \Psi_i \Psi_j \Psi_k \rangle}{\langle \Psi_k \Psi_k \rangle} \end{aligned} \quad (33)$$

for $k = 0, \dots, P$. The explicit, second-order Adams–Bashforth scheme is used for this purpose; we thus have

$$\frac{\mathbf{u}_k^* - \mathbf{u}_k^n}{\Delta t} = \frac{3}{2} \mathbf{H}_k^n - \frac{1}{2} \mathbf{H}_k^{n-1} \quad k = 0, \dots, P, \quad (34)$$

where \mathbf{u}_k^* are the predicted velocity modes, Δt is the time step,

$$\begin{aligned} \mathbf{H}_k \equiv v_0(1 - K' T_{ref}) \nabla^2 \mathbf{u}_k + \sum_{i=0}^P \sum_{j=0}^P C_{ijk} [v_0 K' \nabla \cdot (T_j \bar{\mathbf{S}}(\mathbf{u}_i)) - (\mathbf{u}_i \cdot \nabla) \mathbf{u}_j], \quad (35) \\ C_{ijk} \equiv \frac{\langle \Psi_i \Psi_j \Psi_k \rangle}{\langle \Psi_k \Psi_k \rangle}, \quad (36) \end{aligned}$$

and the superscripts refer to the time level. A similar treatment is used for the energy equation, which is integrated using

$$\frac{T_k^{n+1} - T_k^n}{\Delta t} = \frac{3}{2} J_k^n - \frac{1}{2} J_k^{n-1} \quad k = 0, \dots, P, \quad (37)$$

where

$$J_k \equiv \lambda \nabla^2 T_k - \sum_{i=0}^P \sum_{j=0}^P C_{ijk} \mathbf{u}_i \cdot \nabla T_j. \quad (38)$$

In the second fractional step, we perform a pressure correction to the predicted velocity in order to satisfy the divergence constraints. Specifically, we have

$$\frac{\mathbf{u}_k^{n+1} - \mathbf{u}_k^*}{\Delta t} = -\nabla p_k \quad k = 0, \dots, P, \quad (39)$$

where the pressure fields p_k are determined so that the fields \mathbf{u}_k^{n+1} satisfy the divergence constraints in (14), i.e.,

$$\nabla \cdot \mathbf{u}_k^{n+1} = 0 \quad (40)$$

Combining Eqs. (39) and (40) results in the following system of *decoupled* Poisson equations:

$$\nabla^2 p_k = -\frac{1}{\Delta t} \nabla \cdot \mathbf{u}_k^* \quad k = 0, \dots, P. \quad (41)$$

Similar to the original projection method, the above Poisson equations are solved, independently, subject to Neumann conditions that are obtained by projecting Eq. (39) in the direction normal to the domain boundary [17, 20]. The weak formulation approach outlined in Section 3.5 is used for this purpose. Fast Fourier-based solvers are employed for the inversion of the discrete operators.

5. RESULTS

5.1. Results for P1

Parabolic Inlet Profile

We start by examining a simplified case where a deterministic parabolic velocity profile is imposed at the channel inlet. We use

$$u_{in} = 0, \quad v_{in} = V_{ref} \left[1 - 4 \left(\frac{x}{B} - 0.5 \right)^2 \right], \quad (42)$$

where (u_{in}, v_{in}) are the x - and y -components of the inlet velocity, V_{ref} is the reference velocity, and B is the channel width. The flow is characterized by the Reynolds number based on B , v_0 , and V_{ref} :

$$Re \equiv \frac{B V_{ref}}{v_0}. \quad (43)$$

As mentioned earlier, we are interested in applications with moderate to low Reynolds numbers, so that the flow is stable and laminar.

The (deterministic) solution for steady flow in the channel is the well-known Poiseuille solution [21]

$$u(x, y) = 0, \quad v(x, y) = v_{in}(x), \quad \frac{\partial p}{\partial x} = 0, \quad \frac{\partial p}{\partial y} = -\frac{4\mu V_{ref}}{B^2}, \quad (44)$$

where $\mu = \rho\nu$ is the dynamic viscosity. Thus, when the inlet profile is parabolic, the velocity field is independent of the axial coordinate, y , and, as long as this solution is stable, the velocity is independent of the viscosity as well.

It follows from the above remarks that for the present inlet velocity conditions, an uncertainty in the viscosity would only affect the rate of pressure drop. We have

$$\frac{\partial p}{\partial y} = \frac{-4\rho V_{ref}}{B^2} \nu = \frac{-4\rho V_{ref}}{B^2} (v_0 + v_1 \xi_1) \equiv \frac{\partial p_0}{\partial y} \Psi_0 + \frac{\partial p_1}{\partial y} \Psi_1. \quad (45)$$

Using the definitions $\Psi_0 = 1$ and $\Psi_1 = \xi_1$, and exploiting the orthogonality of the Hermite polynomials we get

$$\frac{\partial p_0}{\partial y} = \frac{-4\rho V_{ref}v_0}{B^2} \quad (46)$$

and

$$\frac{\partial p_1}{\partial y} = \frac{-4\rho V_{ref}v_1}{B^2} = \frac{v_1}{v_0} \frac{\partial p_0}{\partial y}. \quad (47)$$

Furthermore, the variance $\sigma_{\partial p}^2$ of the pressure gradient is given by

$$\sigma_{\partial p}^2 \equiv \left\langle \left(\frac{\partial p}{\partial y} - \frac{\partial p_0}{\partial y} \right)^2 \right\rangle = \left\langle \left(\frac{\partial p_1}{\partial y} \Psi_1 \right)^2 \right\rangle = \left(\frac{\partial p_1}{\partial y} \right)^2. \quad (48)$$

Thus, for Poiseuille flow, the effect of uncertainty in viscosity can be characterized analytically.

The analytical expressions derived above are used to verify the predictions of the stochastic projection scheme. Results are obtained for a channel flow with $Re = 40.62$ and $v_1/v_0 = 0.2$. The simulations are performed in a domain with aspect ratio $H/B = 6$, using a 64×256 computational grid, a time step $\Delta t = 10^{-3} B/V_{ref}$, and a polynomial chaos expansion with $P = 2$. Figure 2 shows the ratio of the computed pressure gradients $\partial p_1/\partial y$ and $\partial p_0/\partial y$, at steady-state, along the centerline of the channel. The results are in excellent agreement with the theoretical prediction in (47). For $y/B > 2$, the analytical and computed results are practically identical, but tiny differences occur near the domain inlet. The maximum relative error between the exact and computed pressure gradient ratios is, however, quite small and falls below 0.05%.

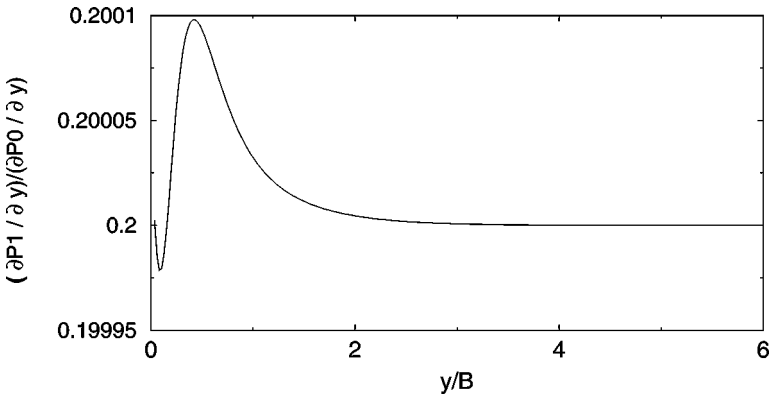


FIG. 2. Pressure gradient ratio $(\partial p_1/\partial y)/(\partial p_0/\partial y)$ along the channel centerline versus the normalized streamwise coordinate y/B . Results are obtained for a channel with $H/B = 6$, $Re = 40.62$, and $v_1/v_0 = 0.2$. The simulation is performed using a grid with 64×256 cells, $\Delta t V_{ref}/B = 10^{-3}$, and a polynomial chaos expansion with $P = 2$.

Uniform Inflow

Here, we consider the case of a uniform inlet velocity profile:

$$u_{in} = 0, \quad v_{in} = V_{ref}. \quad (49)$$

With this inflow condition, the steady (deterministic) flow gradually evolves toward a parabolic Poiseuille profile. The transition reflects the growth of a laminar boundary layer which eventually fills the channel; this delimits the entrance length, whose value depends on the Reynolds number [22]. Within the transition region, the flow field is no longer uniform so that, in the stochastic case, all of the velocity and pressure modes exhibit a nontrivial behavior.

In order to illustrate this behavior, a simulation is performed for a channel with $Re = 81.24$ and $v_1/v_0 = 0.3$. The simulation is performed using a uniform grid with 64×256 , a time step $\Delta t V_{ref}/B = 2 \times 10^{-3}$, and a polynomial chaos expansion with $P = 3$. The unsteady equations are integrated in time until steady conditions are reached. Results are shown in Figs. 3–5, which depict contours of the streamfunction, the streamwise velocity, and the cross-stream velocity, respectively. The streamfunction is reconstructed from the steady velocity field. In each figure, plots are generated for the mean ($k = 0$) as well as modes 1 and 2. The results illustrate the growth of the boundary layer in the entrance region. For the mean flow modes ($k = 0$), entrance effects extend up to $y/B \simeq 4$, and the the corresponding distribution becomes uniform at larger streamwise locations. The streamwise velocity modes

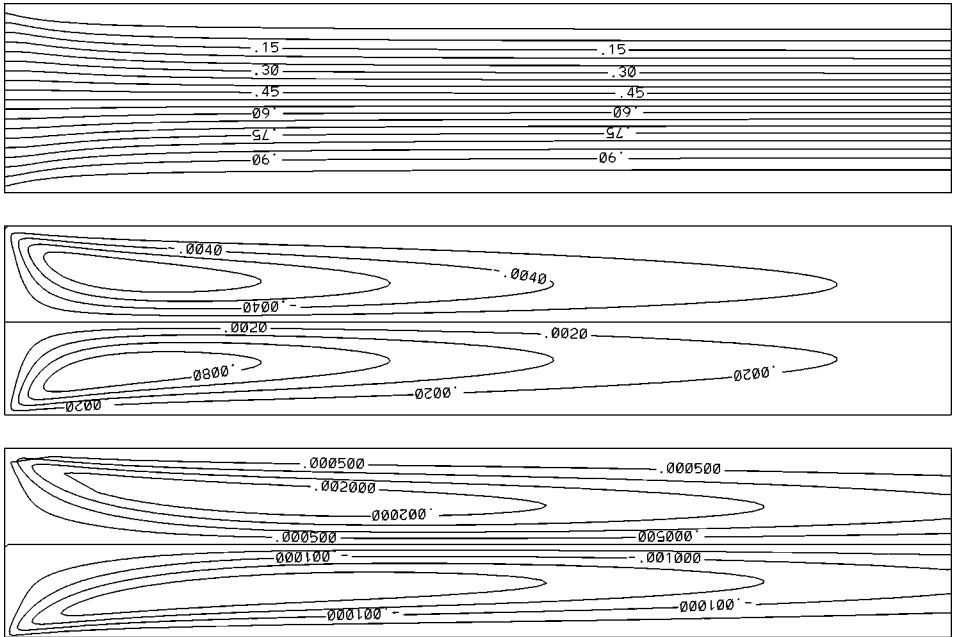


FIG. 3. Contour plots of the streamfunction distribution corresponding to u_0 (top), u_1 (center), and u_2 (bottom). Results are obtained for a channel with $H/B = 6$, $Re = 81.24$, and $v_1/v_0 = 0.2$. The flow is from left to right along the $+y$ -direction; the entire domain ($0 \leq y/B \leq 6$, $0 \leq x/B \leq 1$) is shown. The simulation is performed using a grid with 64×256 cells, $\Delta t V_{ref}/B = 2 \times 10^{-3}$, and a polynomial chaos expansion with $P = 3$.

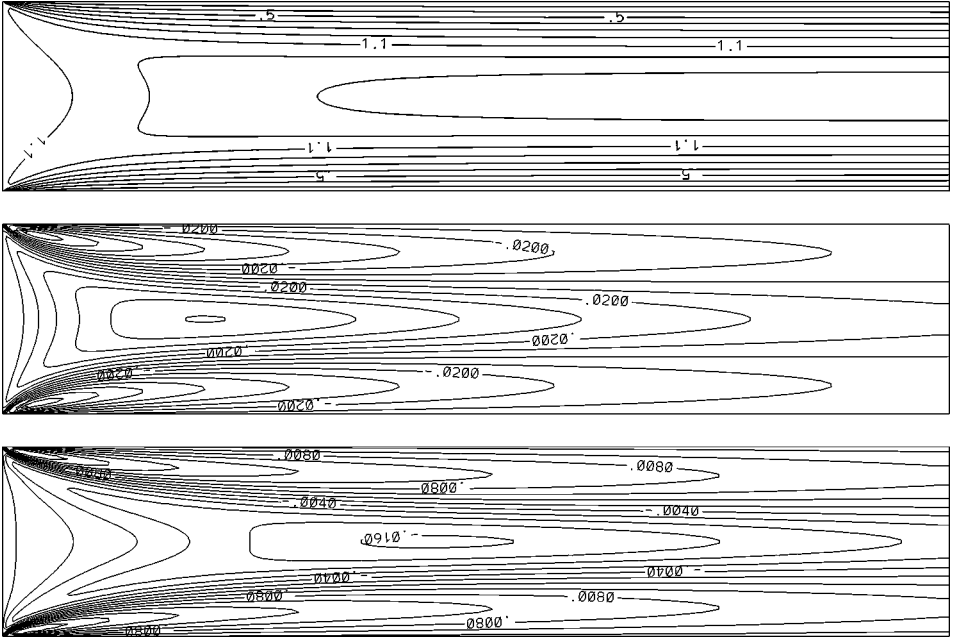


FIG. 4. Contour plots of the streamwise velocity components v_0 (top), v_1 (center), and v_2 (bottom). Same parameters as in Fig. 3.

v_1 and v_2 exhibit appreciable variation up to 4 to 5 channel widths, but the cross-stream velocity modes u_0 , u_1 , and u_2 have negligible values outside the region $0 \leq y/B \leq 3$.

Note that the magnitudes of the fields decrease as k increases, which reflects the fast convergence of the spectral stochastic representation. The stochastic velocity field resulting from the uncertainty in viscosity is dominated by the first mode, which exhibits recirculation regions near the channel entrance that are symmetric with respect to the centerline. Below, we contrast the present solution with results obtained using a nonlinear viscosity law.

5.2. Solution for P2

In this section, we focus once more on a straight channel with uniform inflow but consider that the viscosity is temperature-dependent. The nonlinear viscosity law

$$\frac{\nu(T)}{\nu(T_0)} = 1 + a_1(T - T_0) + a_2(T - T_0)^2 = 1 + a_1T_0 \left(\frac{T}{T_0} - 1 \right) + a_2T_0^2 \left(\frac{T}{T_0} - 1 \right)^2 \quad (50)$$

is assumed, together with a Gaussian, spatially uniform temperature field given by

$$T = T_0 + T_1\xi_1, \quad (51)$$

where T_0 is the mean (reference) temperature and T_1 is the standard deviation. Computations are performed for a channel at $Re = V_{ref}B/\nu_0 = 81.24$, where $\nu_0 \equiv \nu(T_0)$. The coefficients in the nonlinear viscosity law are $a_1T_0 = 9$ and $a_2T_0^2 = 45$. Meanwhile, the

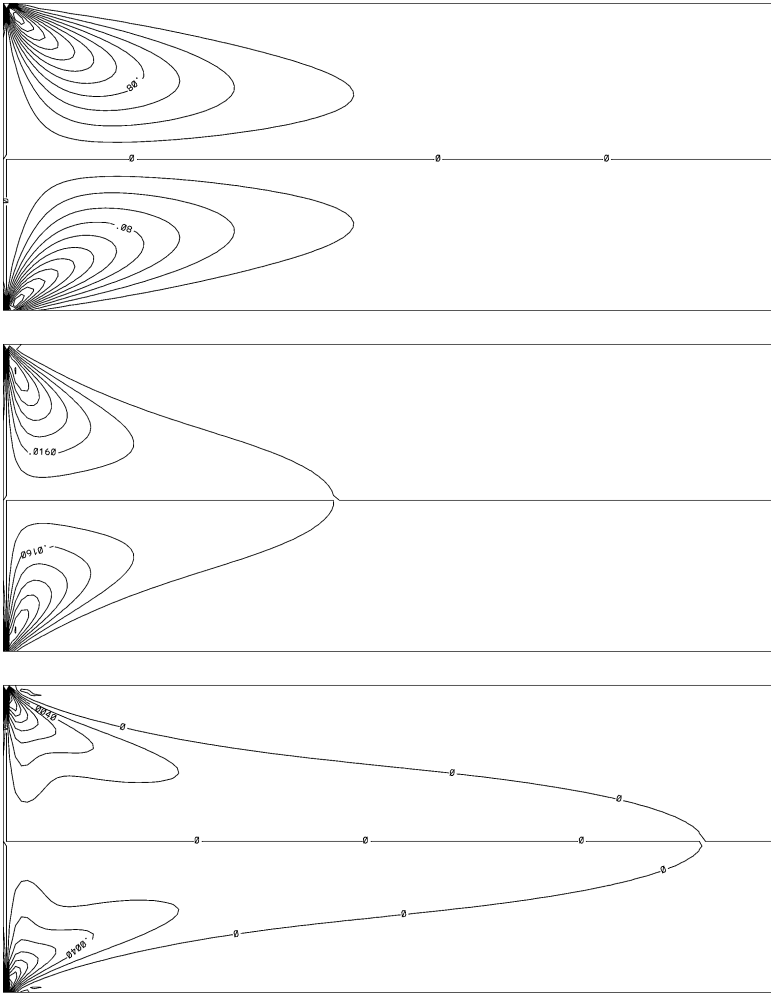


FIG. 5. Contour plots of the cross-stream velocity components u_0 (top), u_1 (center), and u_2 (bottom). Only the first half of the domain ($0 \leq y/B \leq 3$) is shown. Same parameters as in Fig. 3.

standard deviation in the temperature is fixed as $T_1/T_0 = 1/30$. The nonlinear viscosity law is plotted in Fig. 6 together with the scaled probability density function of the temperature. Note for this choice of parameters, linearization of the viscosity law (i.e., setting $a_2 = 0$) would result in the same problem last considered. Thus, the effect of the nonlinearity in the viscosity law can be examined by comparing the results with those given in Section 3.2.

Numerical simulation of the present problem is performed using the same computational grid as in the linear problem, a time step $\Delta t V_{ref}/B = 10^{-3}$, and a polynomial chaos expansion with $P = 3$. Results of the simulation are given in Figs. 7–9, which respectively show the distribution of streamfunction, streamwise velocity, and cross-stream velocity at steady-state. As done earlier, the mean distributions are plotted together with the first two modes. The computed results show that the mean flow behavior in the present case is quite similar to that depicted in Figs. 3–5. In particular, the development of the laminar boundary layer is clearly reflected in the mean streamfunction contours, which are deflected away from

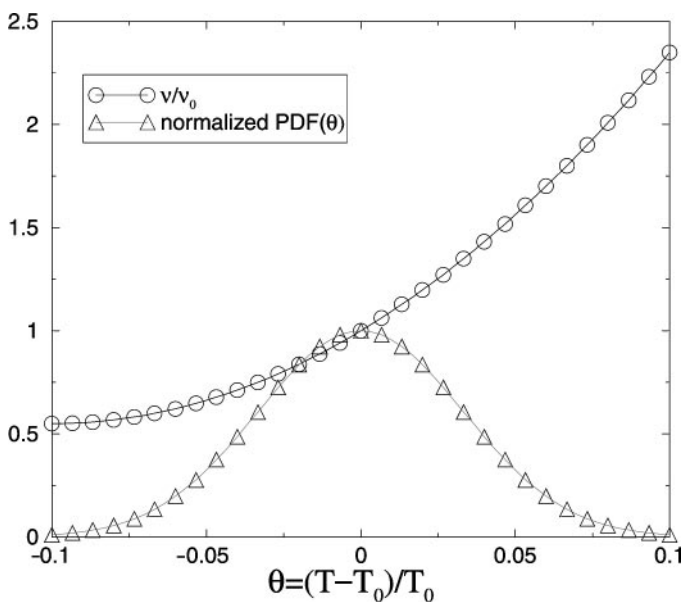


FIG. 6. Dependence of viscosity on the temperature given in Eq. (50) and the scaled probability density function of T .

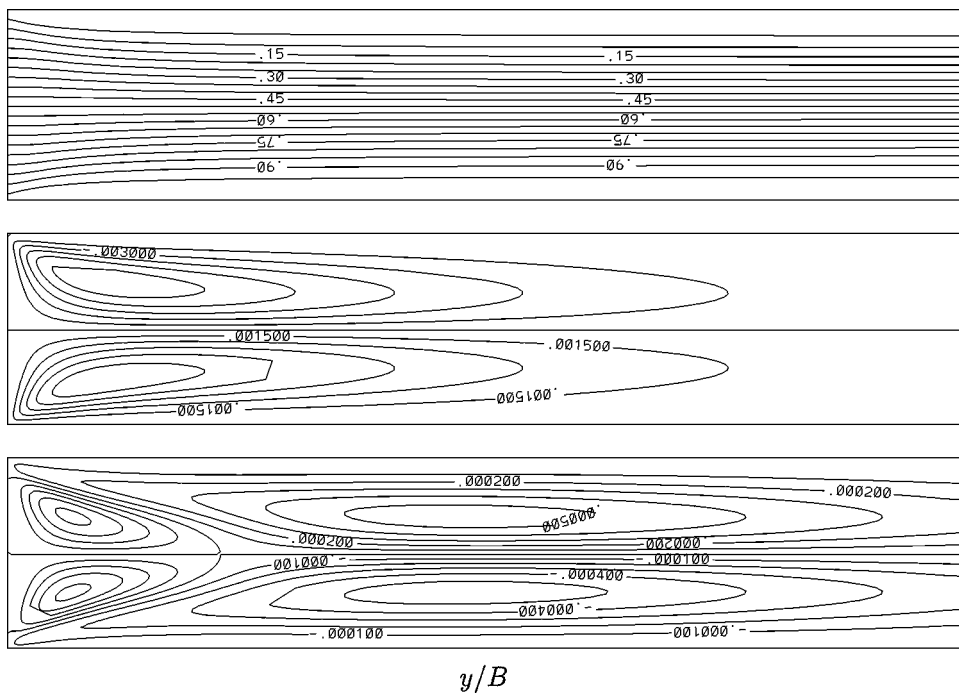


FIG. 7. Contour plots of the streamfunction distribution corresponding to u_0 (top), u_1 (center), and u_2 (bottom). Results are obtained for a channel with $H/B = 6$, $Re = 81.24$, the nonlinear viscosity law and stochastic temperature shown in Fig. 6. The simulation is performed using a grid with 64×256 cells, $\Delta t V_{ref}/B = 10^{-3}$, and a polynomial chaos expansion with $P = 3$.

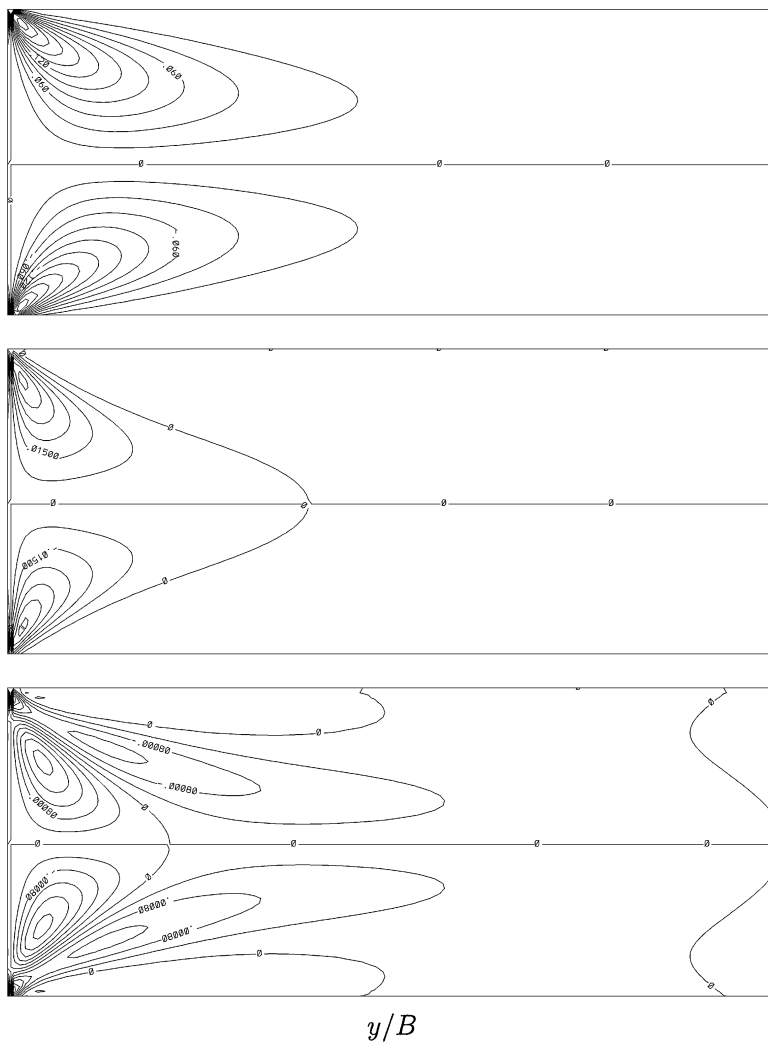


FIG. 9. Contour plots of the cross-stream velocity components u_0 (top), u_1 (center), and u_2 (bottom). Only the first half of the domain ($y/B \leq 3$) is shown. Same parameters as in Fig. 7.

expansion using

$$\sigma_f^2(\mathbf{x}) \equiv \langle (f(\mathbf{x}) - f_0(\mathbf{x}))^2 \rangle = \left\langle \left(\sum_{i=1}^P f_i(\mathbf{x}) \Psi_i \right)^2 \right\rangle = \sum_{i=1}^P f_i^2(\mathbf{x}) \langle \Psi_i^2 \rangle. \quad (52)$$

The results in Fig. 10 show that significant magnitude differences exist between the predictions obtained using linear and nonlinear viscosity laws. In particular, the difference between the two standard deviation fields exhibits peak values that are comparable to those of the corresponding fields. However, unlike our experiences above using the Navier–Stokes solver, the distributions for the two viscosity laws in the Stokes case have a very similar structure. This indicates that nonlinear advective effects can have a substantial impact on the structure of the variance field.

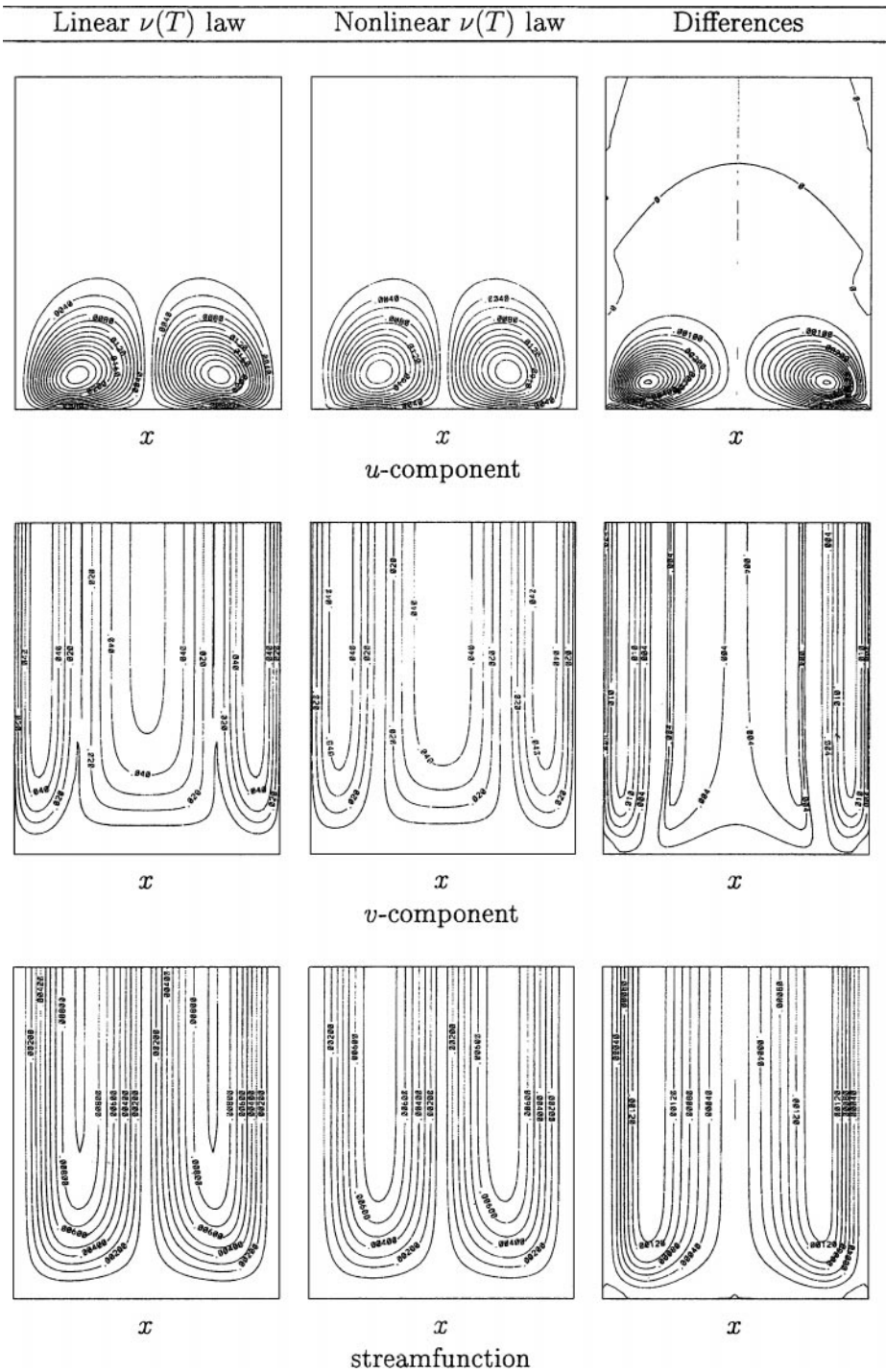


FIG. 10. Contour plots of the standard deviation in the u -component (top), the v -component (center), and streamfunction (bottom). Only the first quarter of the domain ($y \leq 1.5B$) is represented. The results are based on the computed Stokes solution at $t_a = V_{ref}t/B = 1$, using a linear viscosity law with $a_1T_0 = 9$ (left) and a nonlinear viscosity law with $a_1T_0 = 9$ and $a_2T_0^2 = 45$ (middle). The difference between the two standard deviation fields is plotted on the right. In both cases, the solutions are obtained on a grid with 64×256 cells, a time step $\Delta t V_{ref}/B = 10^{-3}$, and a polynomial chaos expansion with $P = 3$.

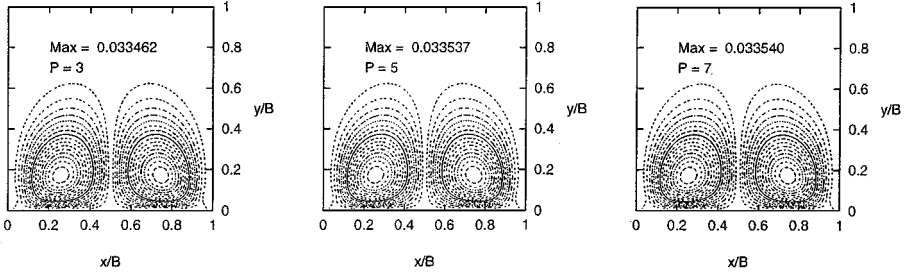
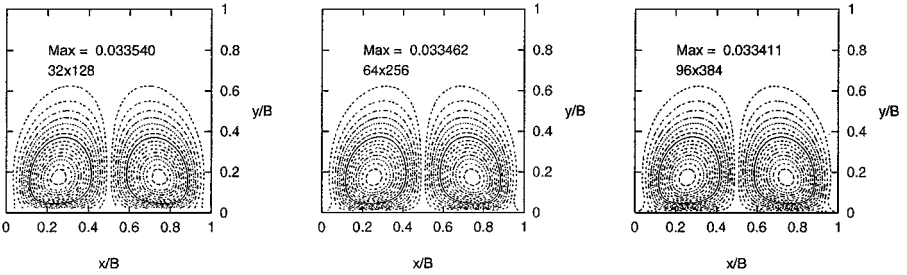
P-refinement*h*-refinement

FIG. 11. Effect of the order P and cell size h on the standard deviation of the u -velocity.

We also use the Stokes problem to investigate the sensitivity of the computed solution with respect to refinement of the computational grid (h refinement) and the order of the polynomial chaos expansion (P refinement). Results of this study are given in Fig. 11, which depicts distributions of standard deviation in the cross-stream velocity u . The P -refinement tests are based on results obtained with $P = 3, 5,$ and 7 , using a 64×256 grid and a time step $\Delta t V_{ref}/B = 10^{-3}$. The h -refinement tests are based on three grids having 32×128 , 64×256 , and 96×384 cells in the x - and y -directions, respectively; in these tests, $P = 3$ and the time steps are $\Delta t V_{ref}/B = 10^{-3}$ for the two coarsest grids and 5×10^{-4} for the finest. The results show that, for the Stokes problem, the standard deviation distribution and peak values are essentially unaffected by the value of P , which demonstrates the fast convergence of the spectral expansion. Figure 11 also shows that the predictions at two finest grid levels are nearly identical, while a slightly higher peak in the standard deviation can be observed for the coarsest grid level. Further examination of the results (not shown) reveals that differences between the coarse level predictions and the more refined computations are restricted to a small region near the channel inlet, and that at larger downstream distances, the coarse grid provides accurate prediction of the solution.

5.3. Solution for P3

Implementation of the stochastic scheme for P3 is illustrated based on simulations of the flow and temperature fields in the double-inlet microchannel schematically shown in Fig. 12. The channel inlet consists of two streams having identical parabolic velocity profiles with peak velocity V_{ref} . The two inlet streams are separated by a plate of thickness D . Thus, the problem can be treated as the wake of a slender bluff body of width D that is located at the center of the channel. The flow is characterized by the Reynolds number

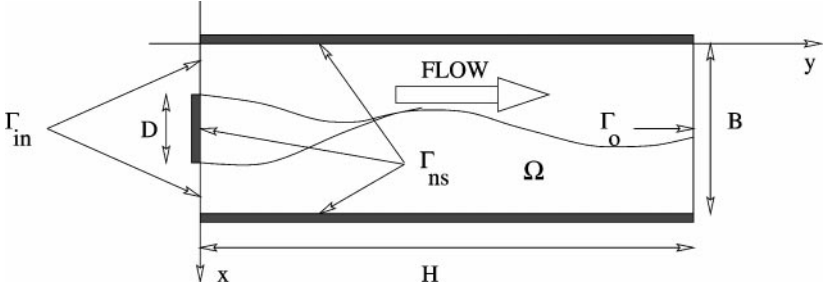


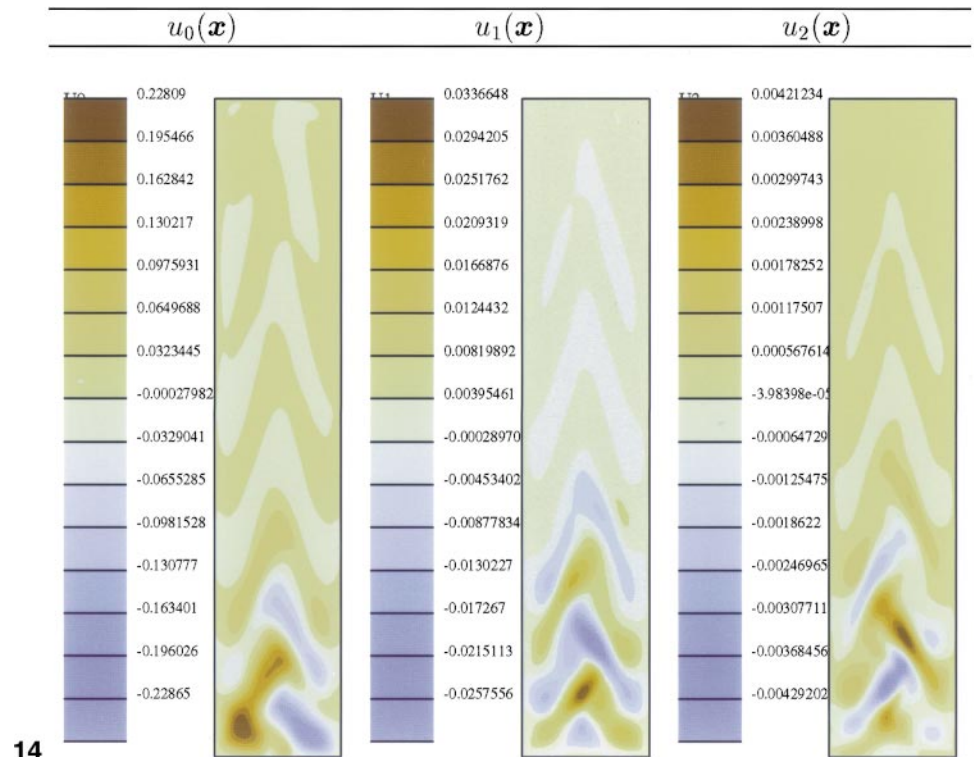
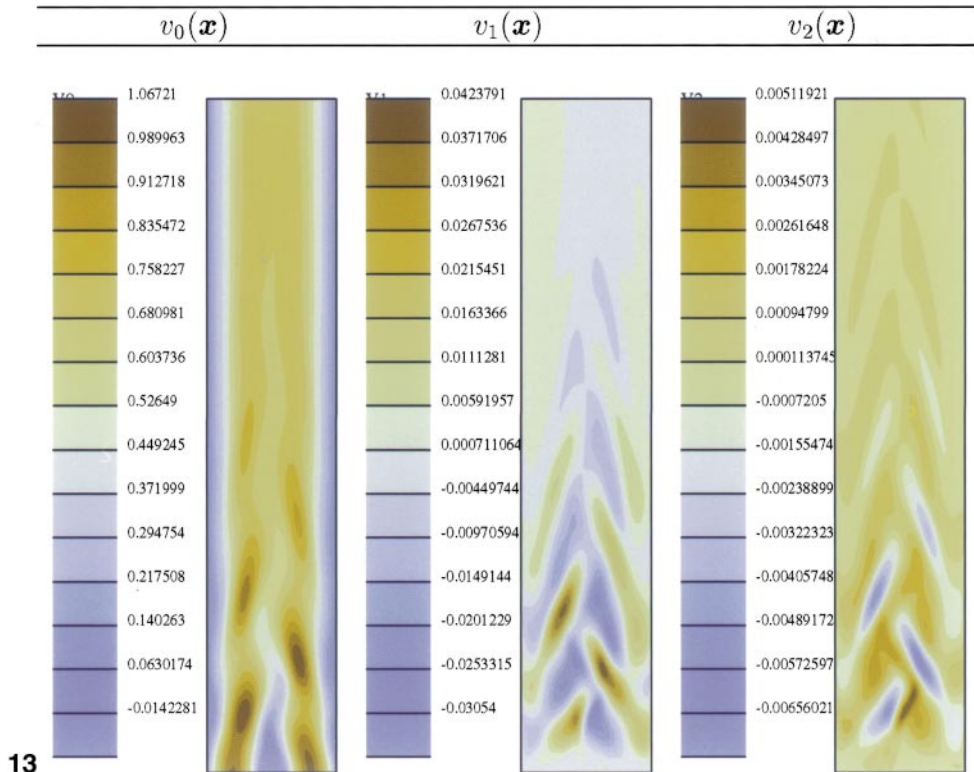
FIG. 12. Schematic illustration of the double-inlet microchannel.

$Re \equiv V_{ref}B/\nu_0$, the blockage ratio D/B , and the Prandtl number λ/ν_0 . As indicated in Section 3.4, $\nu_0 \equiv \nu(T_{ref})$ is the reference viscosity. Note that the blockage ratio and Re can be combined to define a Reynolds number based on the plate thickness, $Re_D \equiv V_{ref}B/\nu_0 = Re D/B$. If Re_D is large enough, the wake of the plate is unstable and periodic vortex shedding is observed, at least for small downstream distances. This situation is considered in the example below. Specifically, we consider a doublet inlet microchannel with blockage ratio $D/B = 0.2$ and Reynolds number $Re = 826$. The Reynolds number based on the plate thickness is $Re_D = 165.2$.

As mentioned in Section 3.4, the uncertainty in this problem is taken to arise as a result of a stochastic temperature boundary condition. Specifically, the temperature of the first inlet is taken to be deterministic and equal to T_{ref} . Meanwhile, the temperature of the second inlet is treated as a random Gaussian variable, with a mean value of T_{ref} and standard deviation of $0.1T_{ref}$. The fluid viscosity is assumed to depend on the temperature according to Eq. (22). This provides a strong coupling between the momentum and energy equations, which is examined in the computations by varying the coupling parameter K' . Specifically, results are obtained using $K = 0.1, 0.2$, and 0.4 , where $K \equiv K'T_{ref}$. In all cases, the Prandtl number $\lambda/\nu_0 = 6$. The computations are performed in a domain with $H/B = 5$, using a 100×352 grid, a time step $\Delta t V_{ref}/B = 2 \times 10^{-3}$, and a polynomial chaos expansion with $P = 3$.

Figures 13 and 14 depict instantaneous contours of streamwise and cross-stream velocity, respectively, at a dimensionless time $tV_{ref}/B = 100$. Plotted in each figure are distributions of the mean instantaneous prediction together with those of modes 1 and 2; results obtained using $K = 0.4$ are used. The distributions of the mean field exhibit the presence of well-defined patches that are arranged in a wavy pattern, which reflects the development of an unstable wake. The results also reveal that the strengths of the vortices shed into the wake gradually decrease with downstream distance. This effect can be clearly observed in Fig. 14, which shows that the magnitude of the cross-stream velocity component decreases with increasing distance from the channel entrance. Thus, the strengths of the vortices decay with y and, for the selected value of the Reynolds number, one would in fact expect a steady parabolic profile at large downstream distances.

Near the channel entrance, the distributions of \mathbf{u}_1 and \mathbf{u}_2 (Figs. 13 and 14) also reveal the presence of well-defined structures that are spatially well correlated with those of the mean field. The velocity magnitudes of the first mode are roughly an order of magnitude higher than those of the second mode. With increasing downstream distance, the magnitudes of \mathbf{u}_1 and \mathbf{u}_2 gradually decrease. This trend is also expected because, at large downstream distances, one would recover a parabolic velocity profile whose strength is solely determined



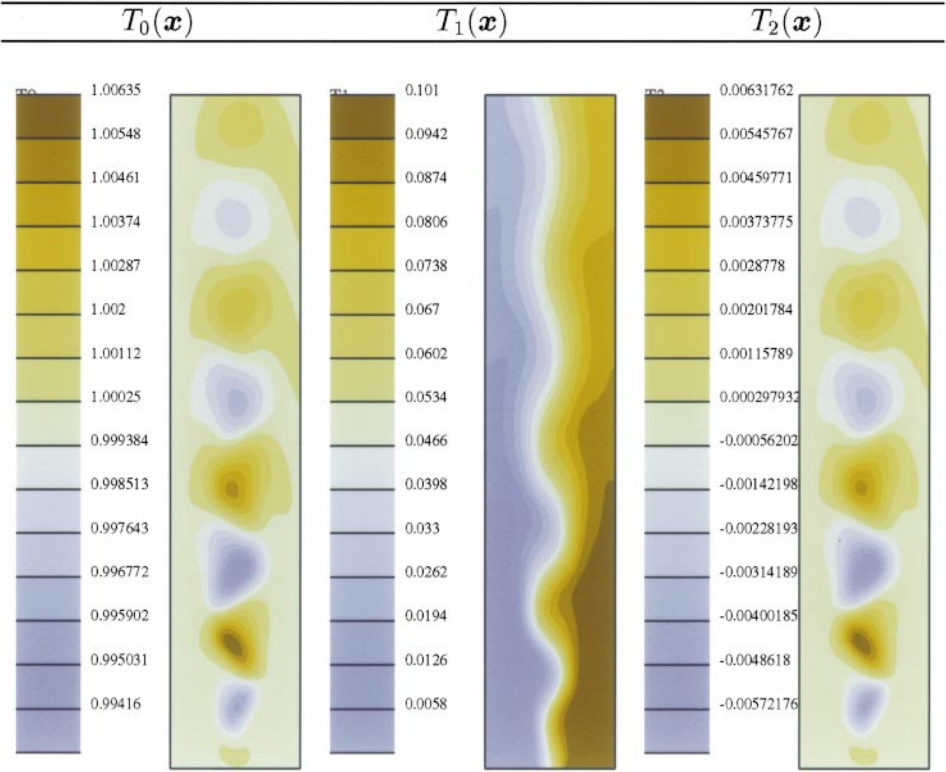


FIG. 15. Instantaneous distribution of T_0 , T_1 , and T_2 at $tV_{ref}/B = 100$. Temperature is normalized using T_{ref} , and results obtained using $K = 0.4$ are used. The flow is from bottom to top, along the $+y$ -direction.

by the volume flux in the channel. In this problem, the volume flux is deterministic, which indicates that all velocity modes with $k \geq 1$ vanish as y increases.

Figure 15 shows instantaneous temperature contours for $K = 0.4$, generated at the same time as in Figs. 13 and 14. The distributions of T_0 and T_2 show the presence of well-defined patches of alternating signs which are consequently arranged at the center of the domain. The strength of the temperature fluctuations within these patches first increases with y , reaches a maximum value around $y/B \sim 2$, and then decreases as we move further downstream. Near the channel entrance, the distribution of T_1 reflects the inlet temperature conditions, which are deterministic for the first inlet and stochastic in the second; thus, T_1 vanishes near the first inlet, peaks near the second, with a gradual transition region at the face of the solid plate. As one moves downstream, the width of this transition region increases leading to the formation of an asymmetric wavy pattern around the wake centerline, with small positive values near the left wall and high values near the right wall. Note that the peak value decreases as one moves downstream while the minimum increases, which

FIG. 13. Instantaneous distribution of v_0 , v_1 , and v_2 at $tV_{ref}/B = 100$. Velocity is normalized using V_{ref} , and results obtained using $K = 0.4$ are used. The flow is from bottom to top, along the $+y$ -direction.

FIG. 14. Instantaneous distribution of u_0 , u_1 , and u_2 at $tV_{ref}/B = 100$. Velocity is normalized using V_{ref} , and results obtained using $K = 0.4$ are used. The flow is from bottom to top, along the $+y$ -direction.

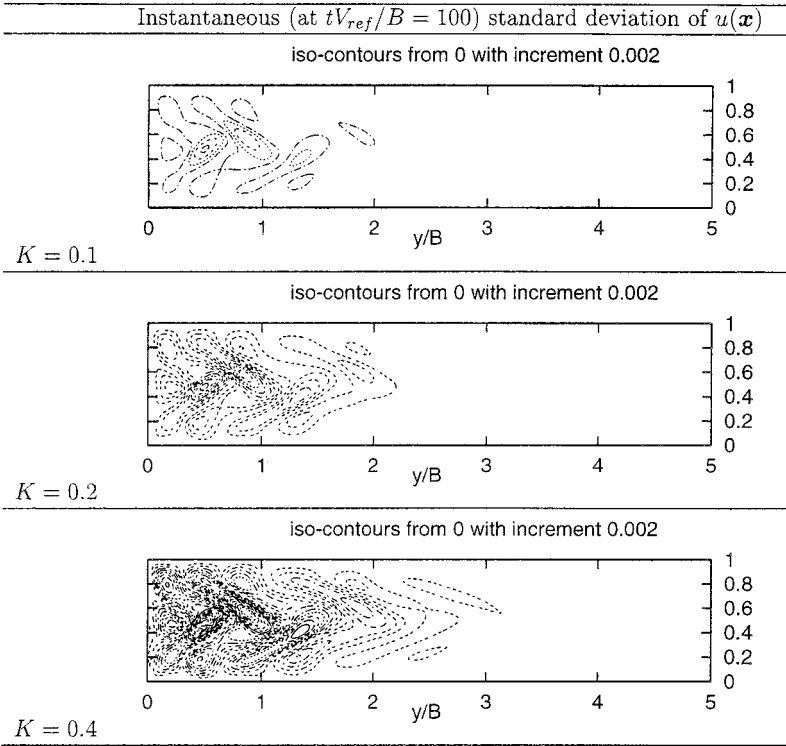


FIG. 16. Instantaneous distribution of the standard deviation of the normalized u -velocity field at time $tV_{ref}/B = 100$; top: $K = 0.1$, middle: $K = 0.2$, bottom: $K = 0.4$.

illustrates how the uncertainty in the boundary condition diffuses as it advected by the flow.

The close correspondence between the temperature fluctuations in the distributions of T_0 and T_2 in Fig. 15 is remarkable, and it is instructive to use the uncertainty representation scheme to interpret the results. The polynomial chaos expansion of the temperature field can be written as

$$\begin{aligned} T(\mathbf{x}, \xi_1) &= T_0(\mathbf{x})\Psi_0(\xi_1) + T_1(\mathbf{x})\Psi_1(\xi_1) + T_2(\mathbf{x})\Psi_2(\xi_1) + \dots \\ &= T_0(\mathbf{x}) + T_1(\mathbf{x})\xi_1 + T_2(\mathbf{x})(\xi_1^2 - 1) + \dots \end{aligned} \quad (53)$$

For $\xi_1 = 0$ the two inlet streams have an identical temperature, T_{ref} . This implies that in this case the temperature field is uniform and everywhere equal to T_{ref} . Using $\xi_1 = 0$ and truncation at $P = 2$, Eq. (53) gives

$$T(\mathbf{x}, \xi_1 = 0) \simeq T_0(\mathbf{x}) - T_2(\mathbf{x}), \quad (54)$$

i.e., the temperature prediction corresponding to $\xi_1 = 0$ is the difference between the mean and second mode. Since, as indicated above, $T(\mathbf{x}, \xi_1 = 0) = T_{ref}$, the fluctuations in T_0 and T_2 should cancel out, so long as the spectral truncation used is valid. This constraint is in fact reflected in the distributions shown in Fig. 15, which also indicates that the (truncated)

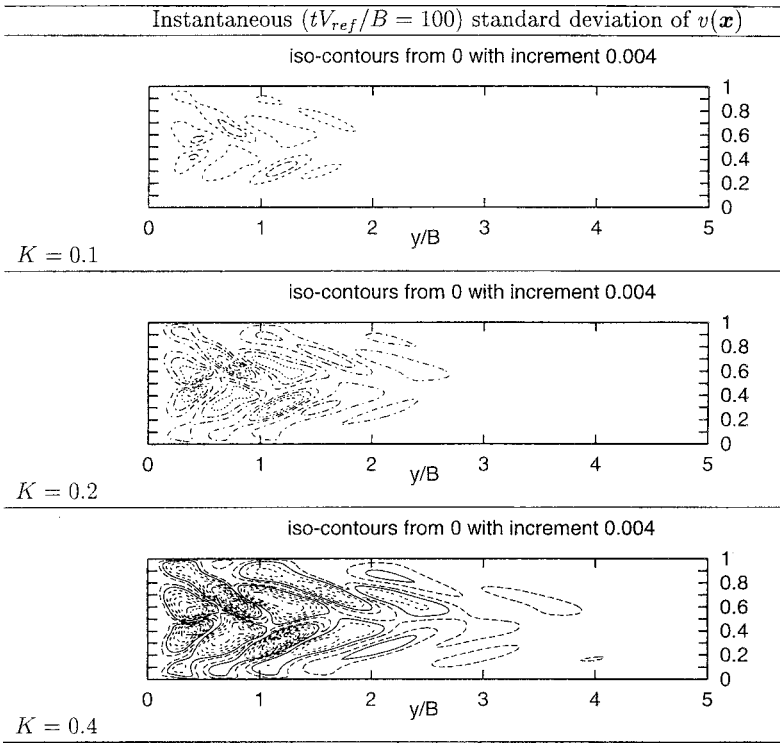


FIG. 17. Instantaneous distribution of the standard deviation of the normalized v -velocity field at time $tV_{ref}/B = 100$; top: $K = 0.1$, middle: $K = 0.2$, bottom: $K = 0.4$.

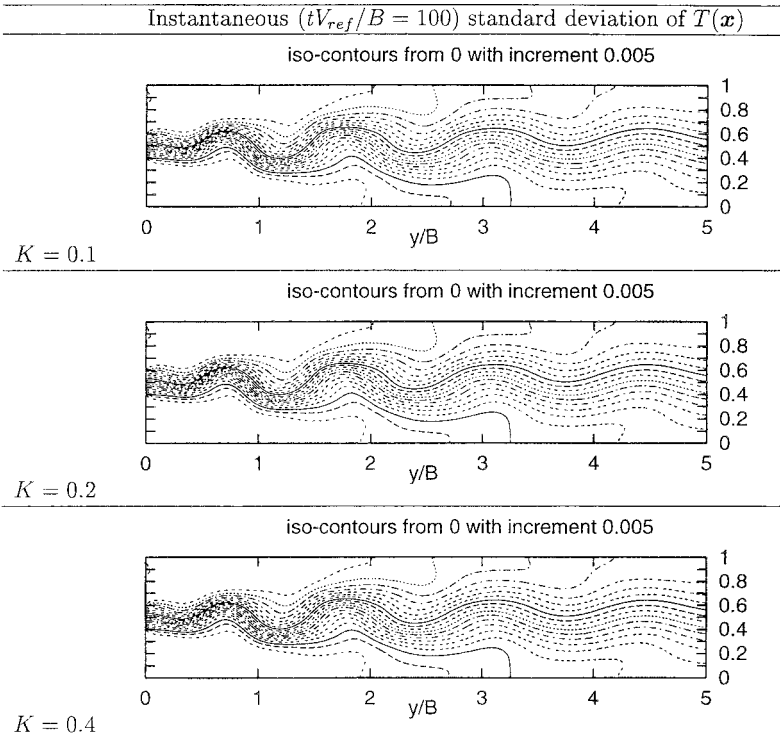


FIG. 18. Instantaneous distribution of the standard deviation of the normalized temperature field at time $tV_{ref}/B = 100$; top: $K = 0.1$, middle: $K = 0.2$, bottom: $K = 0.4$.

higher modes have little impact on the present predictions. One should also note that

$$\langle T(\mathbf{x}) \rangle = T_0(\mathbf{x}) \neq T(\mathbf{x}, \xi_1 = 0), \quad (55)$$

which indicates that the expected temperature field does not coincide with the “deterministic” prediction for $\xi_1 = 0$.

Instantaneous distributions of the standard deviation of u , v , and T are shown in Figs. 16–18, respectively. Plotted are results obtained at $tV_{ref}/B = 100$ using $K = 0.1$, 0.2, and 0.4. The results indicate that the normalized standard deviation for the streamwise (v) and cross-stream (u) velocity components increase with increasing K . As expected, the largest standard deviation values occur in the near wake, where strong vortical structures are present. On the other hand, the contours of the temperature standard deviation exhibit a wavy, asymmetric spreading band near the center of the domain. Unlike the standard deviation of the velocity field, the standard deviation of the temperature is essentially insensitive to the coupling parameter K . Thus, for the present conditions, the propagation of the uncertainty in the temperature field appears to be dominated by the deterministic thermal diffusion coefficient and advection with the (stochastic) mean velocity field.

Profiles of time-averaged values of the streamwise velocity, cross-stream velocity, and temperature are given in Fig. 19. The figure depicts profiles of the first three modes, generated at the streamwise plane $y/B = 1.25$ using simulations with $K = 0.1, 0.2$, and 0.4. The time-averaged profiles reveal trends similar to those observed in the instantaneous distributions.

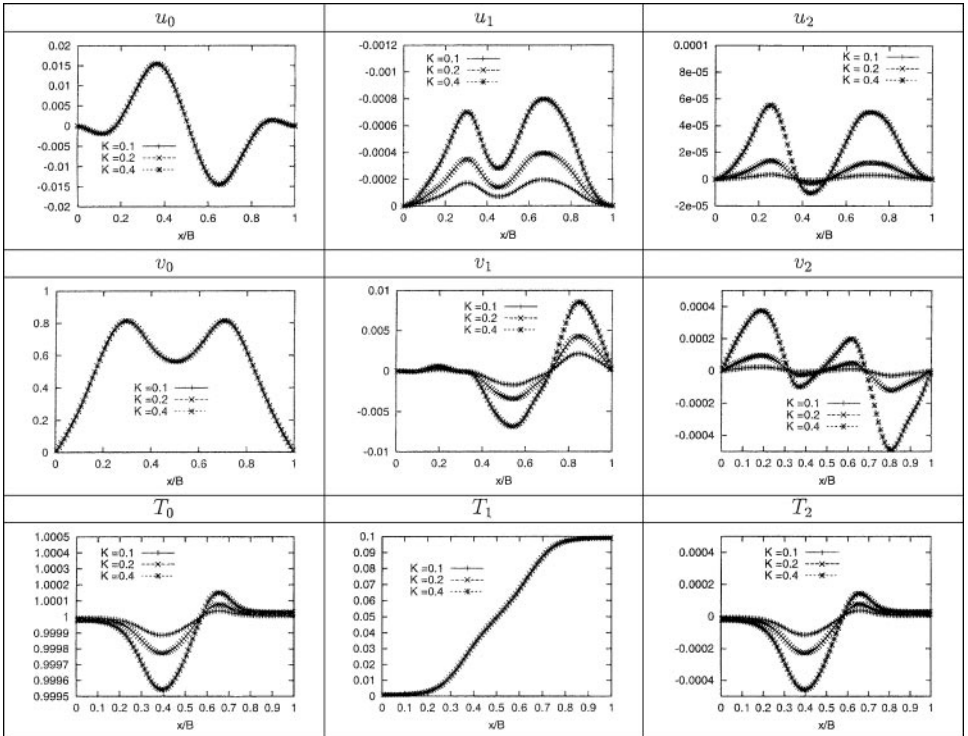


FIG. 19. Time-averaged profiles of U (top), v (center) and T (bottom), at the plane $y/B = 1.25$. The modes correspond to $k = 0$ (left), $k = 1$ (center) and $k = 2$ (right). The curves depict results obtained for $K = 0.1, 0.2$ and 0.4.

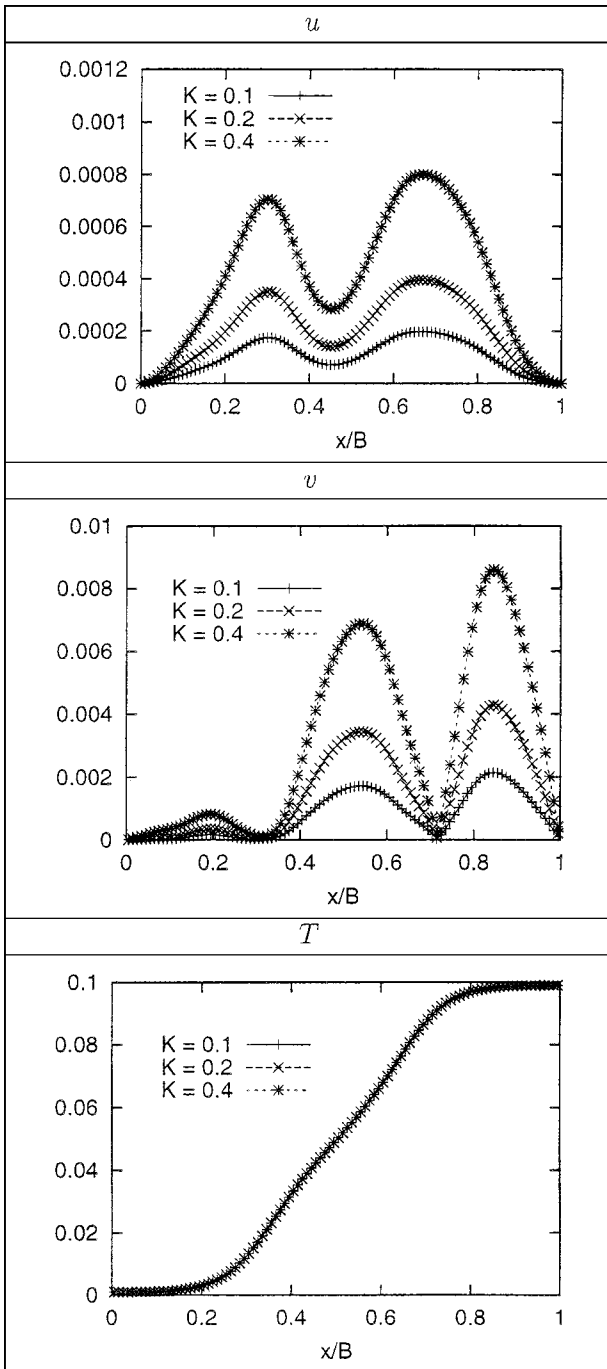


FIG. 20. Time-averaged standard deviation profiles at the plane $y = 1.25B$ for the normalized u -velocity (top), the normalized v -velocity (middle), and the normalized temperature (bottom). The curves depict results obtained for $K = 0.1, 0.2$, and 0.4 .

The mean velocity profiles clearly reflect the development of the unstable wake. Meanwhile, the uncertainty in the velocity field is dominated by the contribution of the first mode, whose peak values are significantly larger than those of the second mode. The results also indicate that as K increases, the uncertainty in the velocity field also increases. This behavior is in sharp contrast with that observed for the temperature profile. The mean temperature prediction exhibits a pronounced dependence on K while the first mode appears to be insensitive to K . As discussed earlier, the fluctuations in the profiles of T_0 and T_2 are quite similar, but are dominated by T_1 which is forced at the inlet boundary. The above trends are also reflected in Fig. 20, which depicts profiles of the normalized standard deviation of the mean velocity components and of temperature. Combined with the results in Fig. 19, it is evident that the contribution of the first mode to the standard deviation is dominant. One can also observe the insensitivity of the temperature standard deviation to the selected value of K , and the strong dependence of the velocity uncertainty on the coupling parameter.

We conclude the discussion with a brief remark on the possible use of the quantitative uncertainty propagation scheme. For instance, in the case of the streamwise profile, the standard deviation is vanishingly small at cross-stream locations ($x/B \sim 0.3$ and $x/B \sim 0.7$) where the mean signal approaches its peak value (compare Figs. 19 and 20). The ratio of the standard deviation to the mean value is clearly minimized at the corresponding locations. Consequently, these positions provide ideal sites for probing the streamwise velocity, in a fashion that minimizes the effect of the uncertainty in stochastic inlet temperature. This illustrates how the stochastic simulation results may be applied to experiment design.

6. CONCLUSION

In this paper, a stochastic scheme is developed which allows the propagation of uncertainty in incompressible Navier–Stokes simulations. The uncertainty representation scheme is based on the polynomial chaos expansion of the solution in terms of the random input data, and on determining the coefficients of this spectral using a Galerkin procedure. The computational uncertainty propagation scheme is constructed by combining the uncertainty representation scheme with a projection method for an incompressible Newtonian fluid. It is shown that this construction results in a coupled system of advection–diffusion equations for the stochastic velocity coefficients, and in a decoupled system of projection steps for the corresponding pressure fields.

Implementation of the stochastic solver is illustrated based on simulations of steady and transient flow in a microchannel at low to moderate Reynolds numbers. Attention is focused on the simplified situation where the uncertain data can be represented as a random variable, and the resulting stochastic scheme is applied to analyze uncertainty in transport properties and boundary conditions. The simulations highlight the efficiency of the stochastic solver, which benefits from the fast convergence of the spectral representation. In particular, for all cases analyzed, it is found that only a small number of terms in the spectral expansion are needed to ensure an accurate representation. The efficiency of the computational scheme also stems from the decoupled structure of the discrete projection steps, which enables us to determine the stochastic solution at the cost of a few deterministic calculations.

As mentioned earlier, the present analysis has been restricted to the case of a single random variable and to incompressible flow of a nonreacting fluid. It should be noted that the first restriction can be immediately relaxed within the present uncertainty representation

framework which has been applied in a variety of more elaborate situations involving random processes, correlated random inputs, and stochastic data with non-Gaussian statistics [23, 24]. It also appears that the incompressible and nonreacting flow assumptions can also be relaxed, in particular by relying on low-Mach-number reacting flow models (e.g., [18, 19]). Extension of the current scheme along these directions is the focus of ongoing efforts.

APPENDIX

The first five polynomials Ψ_j and their corresponding variance $\langle \Psi_j^2 \rangle$ are provided in the following table:

Order j	Polynomial $\Psi_j(\xi)$	$\langle \Psi_j^2 \rangle$
$j = 0$	$\Psi_0(\xi) = 1$	$\langle \Psi_0^2 \rangle = 1$
$j = 1$	$\Psi_1(\xi) = \xi$	$\langle \Psi_1^2 \rangle = 1$
$j = 2$	$\Psi_2(\xi) = \xi^2 - 1$	$\langle \Psi_2^2 \rangle = 2$
$j = 3$	$\Psi_3(\xi) = \xi^3 - 3\xi$	$\langle \Psi_3^2 \rangle = 6$
$j = 4$	$\Psi_4(\xi) = \xi^4 - 6\xi^2 + 3$	$\langle \Psi_4^2 \rangle = 24$

The expectation is defined with respect to the Gaussian measure:

$$\langle f \rangle = \frac{1}{\sqrt{2\pi}} \int_{-\infty}^{\infty} f(\xi) \exp\left(-\frac{\xi^2}{2}\right) d\xi.$$

The polynomials satisfy the orthogonality condition $\langle \Psi_i \Psi_j \rangle = 0$ for $i \neq j$. Expectations of the form $\langle \Psi_i \Psi_j \Psi_k \rangle$ arise in the governing equations. Numerical values for $i, j, k \leq 4$ are given in the following table:

Expectation of $\Psi_i \Psi_j \Psi_k$	value
$\langle \Psi_0 \Psi_0 \Psi_0 \rangle$	1
$\langle \Psi_0 \Psi_1 \Psi_1 \rangle$	1
$\langle \Psi_0 \Psi_2 \Psi_2 \rangle$	2
$\langle \Psi_0 \Psi_3 \Psi_3 \rangle$	6
$\langle \Psi_0 \Psi_4 \Psi_4 \rangle$	24
$\langle \Psi_1 \Psi_1 \Psi_2 \rangle$	2
$\langle \Psi_1 \Psi_2 \Psi_3 \rangle$	6
$\langle \Psi_1 \Psi_3 \Psi_4 \rangle$	24
$\langle \Psi_2 \Psi_2 \Psi_2 \rangle$	8
$\langle \Psi_2 \Psi_2 \Psi_4 \rangle$	24
$\langle \Psi_2 \Psi_3 \Psi_3 \rangle$	36
$\langle \Psi_2 \Psi_4 \Psi_4 \rangle$	192
$\langle \Psi_3 \Psi_3 \Psi_4 \rangle$	216
$\langle \Psi_4 \Psi_4 \Psi_4 \rangle$	1728

Other expectations can be deduced from permutation of indices,

$$\langle \Psi_i \Psi_j \Psi_k \rangle = \langle \Psi_i \Psi_k \Psi_j \rangle = \langle \Psi_j \Psi_i \Psi_k \rangle = \langle \Psi_j \Psi_k \Psi_i \rangle = \langle \Psi_k \Psi_i \Psi_j \rangle = \langle \Psi_k \Psi_j \Psi_i \rangle,$$

and values that are not reported in the table are null.

For a viscosity law of the form

$$\frac{\nu(\xi)}{\nu_0} = 1 + \beta_1 \xi + \beta_2 \xi^2,$$

the first three terms of the polynomial chaos expansion of the incompressible momentum and continuity equations are given by:

$$\text{Mode 0: } \begin{cases} \frac{\partial \mathbf{u}_0}{\partial t} + (\mathbf{u}_0 \cdot \nabla) \mathbf{u}_0 + \nabla p_0 - \nu_0 (1 + \beta_2) \nabla^2 \mathbf{u}_0 \\ = -(\mathbf{u}_1 \cdot \nabla) \mathbf{u}_1 - 2(\mathbf{u}_2 \cdot \nabla) \mathbf{u}_2 + \nu_0 \beta_1 \nabla^2 \mathbf{u}_1 + 2\nu_0 \beta_2 \nabla^2 \mathbf{u}_2 \quad \nabla \cdot \mathbf{u}_0 = 0 \end{cases}$$

$$\text{Mode 1: } \begin{cases} \frac{\partial \mathbf{u}_1}{\partial t} + (\mathbf{u}_1 \cdot \nabla) \mathbf{u}_0 + (\mathbf{u}_0 \cdot \nabla) \mathbf{u}_1 + 2[(\mathbf{u}_1 \cdot \nabla) \mathbf{u}_2 + (\mathbf{u}_2 \cdot \nabla) \mathbf{u}_1] \\ = -\nabla p_1 + \nu_0 (1 + 3\beta_2) \nabla^2 \mathbf{u}_1 + \nu_0 \beta_1 \nabla^2 \mathbf{u}_0 + 2\nu_0 \beta_1 \nabla^2 \mathbf{u}_2 \quad \nabla \cdot \mathbf{u}_1 = 0 \end{cases}$$

$$\text{Mode 2: } \begin{cases} \frac{\partial \mathbf{u}_2}{\partial t} + (\mathbf{u}_2 \cdot \nabla) \mathbf{u}_0 + (\mathbf{u}_0 \cdot \nabla) \mathbf{u}_2 + (\mathbf{u}_1 \cdot \nabla) \mathbf{u}_1 + \nabla p_2 \\ = \nu_0 (1 + \beta_2) \nabla^2 \mathbf{u}_2 + \nu_0 \beta_1 \nabla^2 \mathbf{u}_1 + \nu_0 \beta_2 \nabla^2 \mathbf{u}_0 \quad \nabla \cdot \mathbf{u}_2 = 0. \end{cases}$$

The above expansion is truncated at $P = 2$.

ACKNOWLEDGMENTS

This effort was sponsored by the Defense Advanced Research Projects Agency (DARPA) and Air Force Research Laboratory, Air Force Materiel Command, USAF, under Agreement F30602-00-2-0612. The U.S. government is authorized to reproduce and distribute reprints for governmental purposes notwithstanding any copyright annotation thereon. Computations were performed at the National Center for Supercomputer Applications.

REFERENCES

1. J. M. Hammersley and D. C. Handscomb, *Monte Carlo Methods* (Methuen, London, 1964).
2. S. Ross, *Simulation* (Academic Press, San Diego, 1997).
3. R. G. Ghanem and P. D. Spanos, *Stochastic Finite Elements: A Spectral Approach* (Springer-Verlag, Berlin/New York, 1991).
4. S. Wiener, The homogeneous chaos, *Am. J. Math.* **60**, 897 (1938).
5. R. H. Cameron and W. T. Martin, The orthogonal development of nonlinear functionals in series of Fourier-Hermite functionals, *Ann. Math.* **48**, 385 (1947).
6. R. G. Ghanem and P. D. Spanos, A spectral stochastic finite element formulation for reliability analysis, *J. Eng. Mech. ASCE* **117**, 2351 (1991).
7. R. Ghanem, Probabilistic characterization of transport in heterogeneous porous media, *Comp. Meth. Appl. Mech. Eng.* **158**, 199 (1998).
8. R. Ghanem and S. Dham, Stochastic finite element analysis for multiphase flow in heterogeneous porous media, *Transp. Porous Media* **32**, 239 (1998).

9. B. D. Phenix, J. L. Dinaro, M. A. Tatang, J. W. Tester, J. B. Howard, and G. J. McRae, Incorporation of parametric uncertainty into complex kinetic mechanisms: Application to hydrogen oxidation in supercritical water, *Combust Flame* **112**, 132 (1998).
10. A. J. Chorin, Hermite expansions in Monte-Carle computation, *J. Comput. Phys.* **8**, 472 (1971).
11. F. H. Maltz and D. L. Hitzl, Variance reduction in Monte Carlo computations using multi-dimensional Hermite polynomials, *J. Comput. Phys.* **32**, 345 (1979).
12. D. L. Hitzl and F. H. Maltz, Adaptive estimation procedures for multi-parameter Monte Carlo computations, *J. Comput. Phys.* **37**, 218 (1980).
13. W. C. Meecham and D. T. Jeng, Use of the Wiener–Hermite expansion for nearly normal turbulence, *J. Fluid Mech.* **32**, 225 (1968).
14. S. C. Crow and G. H. Canavan, Relationship between a Wiener–Hermite expansion and an energy cascade, *J. Fluid Mech.* **41**, 387 (1970).
15. A. J. Chorin, Gaussian fields and random flow, *J. Fluid Mech.* **63**, 21 (1974).
16. M. Loève, *Probability Theory* (Springer-Verlag, Berlin/New York, 1977).
17. A. J. Chorin, A numerical method for solving incompressible viscous flow problems, *J. Comput. Phys.* **2**, 12 (1967).
18. H. N. Najm, P. S. Wyckoff, and O. M. Knio, A semi-implicit numerical scheme for reacting flow. I. Stiff chemistry, *J. Comput. Phys.* **143**, 381 (1998).
19. O. M. Knio, H. N. Najm, and P. S. Wyckoff, A semi-implicit numerical scheme for reacting flow. II. Stiff, operator-split formulation, *J. Comput. Phys.* **154**, 428 (1999).
20. J. Kim and P. Moin, Application of a fractional-step method to incompressible Navier–Stokes equations, *J. Comput. Phys.* **59**, 308 (1985).
21. G. K. Batchelor, *An Introduction to Fluid Dynamics* (Cambridge Univ. Press, Cambridge, UK, 1985).
22. R. L. Panton, *Incompressible Flow* (Wiley, New York, 1984).
23. R. Ghanem, The nonlinear gaussian spectrum of lognormal stochastic processes and variables, *ASME J. Appl. Mech.* **66**, 964 (1999).
24. R. Ghanem, Ingredients for a general purpose stochastic finite elements formulation, *Comput. Meth. Appl. Mech. Eng.* **168**, 19 (1999).